scientific reports

Check for updates

OPEN

Correlation analysis of landscape patterns and urban thermal environment in Kunming based on a panel data model

Ting Chen[1], Zhibin Ren[2], Yao Fu[3] & Chang Liu[4]✉

With the development of urbanization, the spatial and temporal distribution characteristics of the urban landscape pattern play a decisive role in the intensity of the urban heat island (UHI) effect. A panel data model was constructed to study the relationship between the UHI effect and landscape pattern in Kunming from 1995 to 2020 at four different scales. The results indicate: (1) The landscape pattern of Kunming changed obviously with time, the artificial patch increased, the natural patch decreased, and the UHI effect became more and more obvious; (2) With an increase in scale, the number of influencing variables continues to grow, and the impact of artificial patches gradually intensifies; (3) The normalized difference water index (NDWI) has the greatest influence on the UHI, and the cooling effect is more obvious with the increase in scale. Unlike previous studies, the spatial configuration of the landscape in Kunming City had a stronger effect on the UHI effect than the landscape grouping and vegetation index; (4) This paper introduces the panel data model into the discussion of the UHI for the first time, providing a new method for better understanding the changing patterns of the urban thermal environment.

Keywords Panel data model, Urban heat island, Landscape pattern, Kunming

Rapid urbanization has exacerbated the UHI effect. The UHI effect refers to the phenomenon where urban temperatures are higher than those in surrounding suburban areas due to urbanization[1]. The UHI effect intensifies the scope and intensity of urban extreme high temperatures, leading to a significant increase in the health risk of urban residents with high temperatures[2–4], which can't be ignored in human physiology and psychology[5]. Recently, scholars have conducted research on the association between COVID-19 and UHI[6]. The alteration of the underlying surface caused by human activities directly affects the absorption of solar radiation by the surface, which is an important way for urbanization to form the UHI effect. This change process of the underlying surface directly reacts to urban landscape patterns[7]. Therefore, the spatiotemporal characteristics of urban landscape patterns, as a direct cause of the UHI effect, to a large extent determine the different intensities of the UHI effect[8,9]. Understanding the correlation mechanism between the UHI effect and landscape patterns is crucial for further deepening the study of the feedback between landscape patterns and ecological processes in urban areas, providing a scientific basis for mitigating the UHI effect, and optimizing landscape patterns.

Many experts have studied the relationship between urban landscape patterns and the UHI effect from different perspectives, including urban size, landscape components, and spatial configuration. As early as the 1970s, Canadian scholar Oke found a positive correlation between urban population size and the UHI effect[10]. In the 21st century, scholars have analyzed the correlation between urban size and the UHI effect based on large samples and multiple temporal remote sensing observations[11–14]. Biophysical parameters obtained through remote sensing monitoring are also a research direction related to the UHI effect. Heinl et al. studied the UHI effect in South Tyrol, Italy, during the summer, using surface normalized difference vegetation index (NDVI) and solar radiation index data, finding that, in combination with irradiance and surrounding land cover, the NDVI has shown in this study to provide a good estimate of UHI intensity[15]. Chen et al. used more remote sensing indices for their study, all showing good correlations with the UHI. Currently, dozens of remote sensing indices can be utilized[16].

[1]Faculty of Soil and Water Conservation, Southwest Forestry University, Kunming 650024, China. [2]Northeast Institute of Geography and Agroecology, Chinese Academy of Sciences, Changchun 130102, China. [3]School of Geography and Land Engineering, Yuxi Normal University, Yuxi 653100, China. [4]Faculty of Forestry, Southwest Forestry University, Kunming 650024, China. ✉email: missliu@swfu.edu.cn

In addition to studies on urban size and remote sensing parameters related to the UHI effect, landscape patterns also serve as an excellent means of characterizing UHI. Consequently, many experts consider landscape metrics as key research parameters related to UHI. Relevant studies indicate that impervious surfaces are the primary cause of increased LST, while green spaces and water bodies can effectively reduce LST. However, it is impractical to infinitely expand the area of green spaces and water bodies in cities due to the unique conditions in China. Therefore, researchers have begun to study the impact of the structural composition and spatial configuration of landscapes on LST[17]. Landscape pattern indices are an effective method for quantitatively studying a series of information related to landscape composition characteristics, spatial configuration, and their dynamic changes[18]. Landscape indices (such as patch size, number, and shape) are important factors influencing LST. Previous research has proven that optimizing the landscape configuration of water bodies and green spaces is crucial for mitigating UHI[19,20].

However, even for the same city, some studies have shown opposite conclusions. In a case study in Beijing with varying sampling granularities, only the patch density (PD) was significantly correlated with LST at all granularities. On the other hand, a summer study in Shanghai showed that indices such as LSI and PD were not related to LST[21]. Similarly, in the analysis of the association between green space landscape configuration and cooling effects, some studies have found that simple-shaped and concentrated green patches have better cooling effects, while other studies have concluded[22,23] that complex-shaped and dispersed green spaces have lower temperatures and stronger cooling effects[24,25].

The causes of the above contradictions may include: (1) differences in the scale of analysis units due to different pixel sizes; (2) lack of dynamic analysis of the same city over multiple periods; (3) different statistical analysis methods used in various studies; (4) neglect of the mutual influence among various factors on the study[26,27]. To eliminate these contradictions, Li et al. used the WRF model and geospatial methods to dynamically analyze the relationship between near-surface temperature (NST) and landscape pattern at the urban agglomeration scale. They obtained dynamic correlation coefficients reflecting the real impact of landscape pattern changes on NST, while static correlation coefficients indicated the expected impact of landscape pattern changes on NST[28]. Despite the abundant research results, there are still some deficiencies: Firstly, the choice of study areas has primarily focused on large cities both domestically and internationally, lacking systematic research on inland plateau lake cities like Kunming. Due to its unique geographical environment and climatic conditions, the UHI in Kunming differs from other cities, making it more valuable for study. Secondly, although there are dynamic studies on the relationship between landscape patterns and thermal environments, there is a lack of multi-scale dynamic correlation research. Lastly, current studies often use single cross-sectional time samples when using long-term temporal scale samples, constructing statistical models for different periods. This approach can lead to repetitive work and increased time costs.

In the modern theoretical system of econometrics, a specific class of model known as the panel data model exists. Compared to other models, their advantages are as follows: (1) A large dataset can extract more rich information and improve the accuracy of estimates, reducing the possibility of collinearity among variables, increasing the degrees of freedom of model estimates, and enabling the construction and testing of more complex variable structural relationships[29].(2) In addition to the cross-sectional dimension, panel data has a time dimension, examining the time variation trend of effects and conducting dynamic analysis.(3) The panel data model can reduce the confusion of individual differences and time trends, enhancing the reliability and validity of the data[30–33].

In summary, this paper takes Kunming City as the research object and adopts the method of establishing a panel data model to study the relationship between urban landscape patterns and the UHI effect on four scales over the period from 1995 to 2020. This approach helps enrich the exploration of the coupling mechanism between landscape patterns and ecological processes at the theoretical level, promotes the refinement of the core of urban landscape ecology theory and methodologies, and provides practical landscape optimization approaches to enhance the adaptability of Chinese urbanization to climate change.

Materials and methods

Study area

Kunming is located in the southwestern region of China, in the central part of the Yunnan-Guizhou Plateau, in the north-central area of Yunnan Province. Its geographic coordinates range from approximately 102°10' to 103°40' east longitude and 24° 23′ to 26° 22′ north latitude. The city lies to the south of Dianchi Lake, surrounded by mountains on three sides. The general topography features higher elevations in the north, lower elevations in the south, with a central uplift, and lower terrain on the east and west sides. The predominant landforms include the basin karst plateau, followed by the red highland plateau. Elevations across the majority of the area range from 1500 to 2800 m. River erosion has a relatively mild impact. Kunming experiences a subtropical-highland monsoon climate at low latitudes in the northern hemisphere, characterized by the influence of the warm and moist southwest monsoon from the Indian Ocean. As a result, the city enjoys long sunshine hours, a short frost period, an annual average of around 2200 h of sunshine, and an annual precipitation of 1035 mm. The climate exhibits typical temperate characteristics, with temperatures in the urban area ranging from 0 to 29 °C. Kunming exhibits the most minimal annual temperature variation within the nation, characterized by an average yearly temperature of approximately 15 °C. The hottest month has an average temperature of around 19 °C, while the coldest month has an average temperature of around 8 °C. Historical extreme temperatures recorded in Kunming include a maximum of 31.2 °C and a minimum of -7.8 °C. According to the seventh national census report, Kunming has a permanent population of 8,460,088, with 5,343,566 residing in the main urban area, accounting for 63.16%. The "13th Five-Year Plan for New Urbanization Development in Kunming" points out that by 2020, the urbanization rate of the permanent population in the main urban area will reach approximately 73%. Over the past 30 years, Kunming has undergone rapid urbanization, with the main urban area being

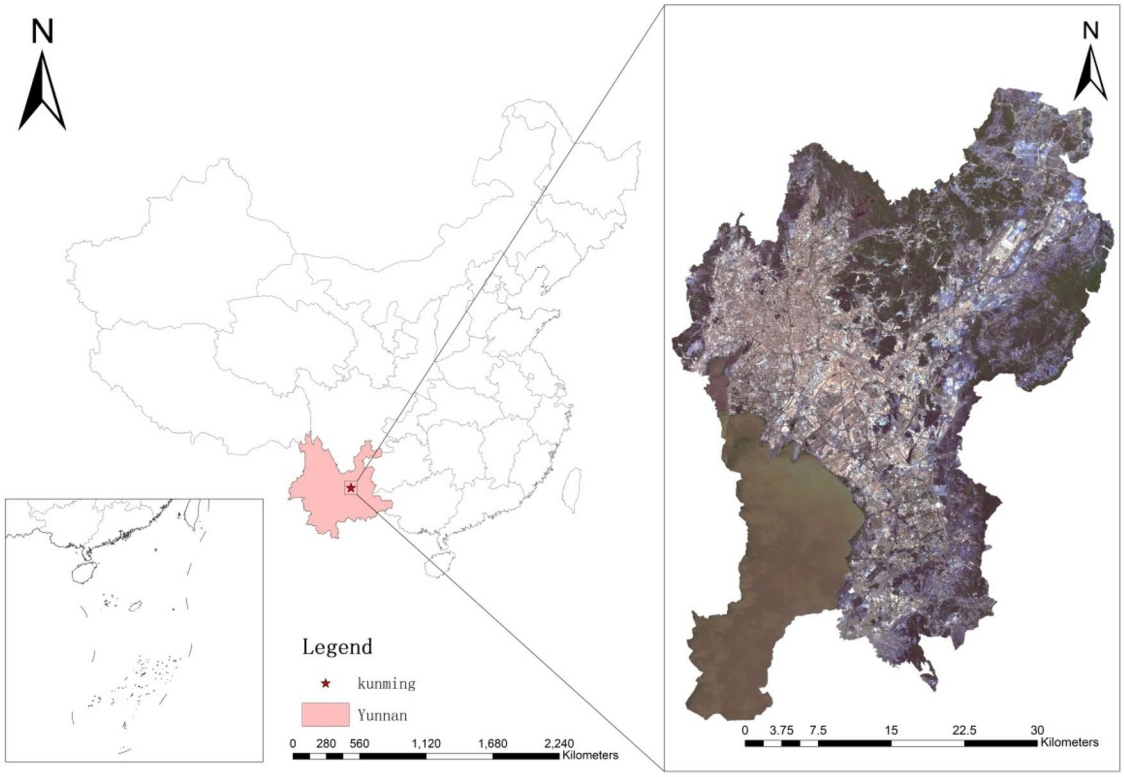

Fig. 1. Location of the study area. The graph was created using ArcGIS10.7 (https://www.arcgis.com), The base map was from the standard map with review number GS (2022) 2764 downloaded from the website of Standard Map Service of the Ministry of Natural Resources, with no modification of the base map (http://bzdt.ch.mnr.gov.cn/).

Scene ID	Sensor	Acquisition date	Cloud cover (%)	Number of band
LT51290431995109BKT01	TM	1995-04-19	2.00	7
LT51290432001093BJC00	TM	2001-04-03	2.00	7
LT51290432005120BJC00	TM	2005-04-30	4.00	7
LT51290432010134BKT01	TM	2010-05-14	4.00	7
LC81290432015148LGN01	OLI/TIRS	2015-05-28	0.70	11
LC81290432020130LGN00	OLI/TIRS	2020-05-09	3.67	11

Table 1. Data description.

the primary region for talent and resource aggregation. As Kunming's urban space continues to expand and population density increases, while this urbanization has promoted socio-economic development, it has also negatively impacted the city's thermal environment. (Fig. 1).

Research Data

Landsat data for Kunming City for the years 1995, 2000, 2005, 2010, 2015, and 2020 were downloaded from the United States Geological Survey (USGS) (http://earthexplorer.usgs.gov/). Generally, the UHI effect is more pronounced closer to the summer, but Kunming experiences cloudy and rainy conditions during the summer, resulting in poor data quality. Research indicates that data acquired in the spring show minimal variation in climatic conditions such as temperature, humidity, and cloud cover, reducing the atmospheric background's impact on satellite image quality[34]. Therefore, the selected data are primarily from April to May. If no cloud-free satellite images were available for a given year, images from adjacent years with low cloud cover (below 5%) were used (Table 1). Accuracy verification was conducted using contemporaneous MOD11A1 temperature products, which have a spatial resolution of 1000 m and are sourced from NASA (https://ladsweb.modaps.eosdis.nasa.gov/). The temporal scope is from 2000 to 2020, so the 1995 data were not validated.

Year	Overall accuracy (%)	Kappa cofficient
1995	97.43	0.95
2001	92.64	0.88
2005	95.69	0.92
2010	92.34	0.89
2015	93.55	0.90
2020	92.21	0.88

Table 2. The accuracy of classified LULC.

Index	Description	Unit	Range
Albedo	Reflect the overall reflectance of ground objects to visible light and near-infrared light	None	[0,1]
SAVI	A vegetation index that adjusts for soil surface reflectance	None	[0,1]
NDVI	This index is a measure of healthy, green vegetation	None	[-1,1]
NDWI	An index used for water body detection and extraction in remote sensing images	None	[-1,1]
EVI	An optimized vegetation index that can account for atmospheric effects and vegetation background signals	None	[-1,1]
NDBI	An index used for building extraction in remote sensing imagery	None	[-1,1]
PD	Measuring the density of patches in a landscape	Patches/ha	[0,+∞]
LPI	Measuring the proportion of the largest patch area relative to the entire landscape in a professional context	%	[0,100%]
ED	The ratio of the total perimeter length of all patches to the total area of the entire landscape	m/ha	[0,+∞]
LSI	Focusing on measuring the geometric shape characteristics of patches	None	[1,+∞]
AREA_MN	Describing the typical size range of various types of patches within a landscape in a professional context	ha	[0,+∞]
GYRATE_MN	Measuring the spatial expansion potential and shape complexity of patches within a landscape in a professional context	ha	[0,+∞]
PARA_MN	Measuring the shape complexity of patches in a landscape within a professional domain	m/ha	[0,+∞]
PAFRAC	Measuring the average shape complexity of all patches in a landscape	None	[1,2]
CONNECT	Evaluating the connectivity of patches of the same type within a landscape in a professional context	None	[0,1]
AI	Describing the degree of aggregation of patches of the same type within a landscape in a professional context	None	[0,1]
PLAND	An index describing the proportion of a specific landscape type within the entire landscape	%	[0,100%]
COHESION	Measuring the spatial connectivity of patches within a landscape in a professional context	None	[0,1]
DIVISION	Evaluating the degree of fragmentation of patches within a landscape in a professional context	None	[0,1]
SHEI	Assessing the evenness of distribution of various patch types within a landscape	None	[0,+∞]
SHDI	Measuring the diversity of landscape types within a given area.	None	[0,+∞]

Table 3. Characteristic index.

Research methods

(1) Image preprocessing

The research data spans 25 years, and some of the data are affected by clouds, so the preprocessing of remote sensing images mainly includes radiometric calibration, image registration, cropping, and atmospheric correction.

(2) Extraction of vegetation indices and landscape characteristics

The vegetation index is a simple, effective, and empirical measure of the vegetation status in the study area. The landscape index is an index that evaluates the landscape in an area, and the index is calculated based on of land use type. According to the national standard "Classification of Current Land Use Status," Landsat remote sensing imagery was classified using object-oriented and visual interpretation methods. The land was categorized into four types: green space, building space, water bodies, and unused land. High-resolution images from Google Earth were used as a reference layer to evaluate the classification accuracy (Table 2), the classification accuracy for all categories exceeded 80%, meeting the required precision for extracting landscape pattern indices.

Building upon this, and referring to previous research, 20 indices, including vegetation indices and landscape indices (Table 3), were extracted at four scales (500 m, 1000 m, 1500 m, and 2000 m). The selection of indices not only considers relevant characteristics of vegetation but also includes area-based indices, structure-proportion indices, shape indices, and considerations for the influence of water bodies on surface temperature. When calculating the Albedo index, the applicability of narrow vegetation areas in urban regions needs to be considered. Landsat data can provide long-term time series data, multiple spectral bands, and a 30-meter resolution, which is effective for identifying large areas of vegetation. This makes it suitable for extensive area and urban studies[35,36].

(3) Extraction of land surface temperature (LST)

Through numerous studies on the extraction of LST, it can be found that there are many methods for extracting LST, primarily including the single-window algorithm[37], radiation transfer equation method[38], and single-channel algorithm. Some studies have compared the results of LST retrieval using the single-window algorithm, radiation transfer equation method, and single-channel algorithm. They found that when using TM data, the single-window algorithm had the highest accuracy, while the single-channel algorithm had the lowest accuracy. Conversely, when using ETM + data, the single-channel algorithm showed the highest accuracy, and the single-window algorithm had the lowest. For Landsat 8 TIRS data, the single-channel algorithm again had the highest accuracy, while the radiation transfer equation method had the lowest[39]. Moreover, in practical applications, the radiation transfer equation method struggles to obtain atmospheric profile data such as atmospheric transmittance before the year 2000. The single-window algorithm requires surface temperature data near the ground (approximately 2 m) at the time of satellite overpass to calculate the average atmospheric effect temperature. The remote sensing data used in the study spans from 1995 to 2020 and lacks temperature data at the time of the satellite overpass. Therefore, the single-channel algorithm is chosen for LST retrieval. The single-channel algorithm, proposed by Jiménez – Muñoz and Sobrino[40–42], is a universal method for retrieving surface temperature and was improved in 2009. The algorithm formula is as follows:

$$\mathrm{LST} = \gamma \cdot \left[\varepsilon^{-1} \cdot (\varphi_1 \cdot \mathrm{L}_S + \varphi_2) + \varphi_3\right] + \delta \tag{1}$$

$$\gamma = \left[\frac{C_2 \cdot L_S}{T^2}\left(\frac{\lambda^4}{C_1} L_\mathrm{S} + \lambda^{-1}\right)\right]^{-1} \tag{2}$$

$$\delta = -\gamma \cdot \mathrm{L} + \mathrm{T} \tag{3}$$

In the equation, LST represents land surface temperature, measured in Kelvin (K); ε is the emissivity of the land surface; Ls is the radiance, measured in W/(m^2 sr μm); T is the brightness temperature, measured in Kelvin (K); λ is the effective wavelength of the sensor; c_1 and c_2 are constants($c_1 = 1.19104 \times 10^8 \mathrm{w} \cdot \mu\mathrm{m}^4 \cdot \mathrm{m}^{-2} \cdot \mathrm{sr}^{-1}$, $c_2 = 14387.685\ \mu\mathrm{m} \cdot \mathrm{k}$); φ_1, φ_2, φ_3 are atmospheric functions, related to the atmospheric water vapor content on the day of imaging, The calculation formula is as follows:

$$\begin{aligned} \varphi_1 &= \rho_{11}\omega^2 + \rho_{12}\omega + \rho_{13} \\ \varphi_2 &= \rho_{21}\omega^2 + \rho_{22}\omega + \rho_{23} \\ \varphi_3 &= \rho_{31}\omega^2 + \rho_{32}\omega + \rho_{33} \end{aligned} \tag{4}$$

In the formula, ρ_{ij} is obtained through fitting. Jiménez-Muñoz and Xu Hanqiu et al. used the atmospheric radiative transfer software MODTRAN4.0 and the least squares method to fit and derive the relationship coefficients between the three atmospheric functions of Landsat data and atmospheric water vapor content, as shown in Table 4.

(4) Variable selection

Stepwise multiple regression analysis is used to determine the relative importance of each indicator. The optimal result is based on the highest correlation coefficient (R^2). Through stepwise regression, the explanatory variables retained in the final model are both significant and perform better in multicollinearity. The calculation formula is as follows:

$$\mathrm{Y_i} = \beta_0 + \beta_1 \mathrm{X}_1 + \beta_2 \mathrm{X}_2 + \cdots + \beta_\mathrm{n} \mathrm{X}_\mathrm{n} \tag{5}$$

Where Y is the LST, β_0 is the constant term, $\mathrm{X_i}$(i = 1,2,…,n)are the extracted indicators, and β_i (i = 1,2,…,n) are the standardized regression coefficients.

Remote sensing data	$\rho_{ij}(i = 1, 2, 3; j = 1, 2, 3)$		
Landsat ETM+	0.14714	-0.15583	1.12340
	-1.18360	-0.37607	-0.52894
	-0.04554	1.87190	-0.39071
Landsat TM	0.04597	0.06269	1.00818
	-0.32297	-2.16801	0.55698
	-0.06397	1.69324	0.45747
Landsat TIRS	0.04019	0.02916	1.01523
	-0.38333	-1.50294	0.20324
	0.00918	1.36072	-0.27514

Table 4. Relationship coefficients between atmospheric functions and atmospheric water vapor content.

(5) Ordinary least squares (OLS) regression model

The OLS method is to minimize the sum of the squares of all data deviations. It includes simple linear regression, polynomial regression, and multiple linear regression. A multiple linear regression model, which contains multiple explanatory variables, can be used to explain the linear relationship between LST and the selected variables. The model's interpretability is determined using the regression coefficient R^2 and residual analysis. The mathematical model is:

$$Y_i = \beta_0 + \beta_1 X_{i1} + \beta_2 X_{i2} + \cdots + \beta_p X_{ip} + \varepsilon_i \quad (6)$$

Where β_0 is the intercept; β_j(j = 1,2,…,p)is the regression coefficient; p is the number of observations, with 6091 at the 500 m grid scale, 1598 at the 1000 m grid scale, 738 at the 1500 m grid scale, and 434 at the 2000 m grid scale.

(6) Panel Data Model

The panel data model, also known as the time series-cross-sectional data model, is a combination of cross-sectional data and time series data. From the cross-sectional perspective, it consists of cross-sectional data formed by several individuals at a certain point in time, and from the longitudinal perspective, it is a time series. This data structure can effectively reduce the collinearity of explanatory variables and the loss caused by missing variables. The calculation formula is:

$$y_{it} = \beta_0 + X_{it}\beta + \varepsilon_{it} \quad (7)$$

Where $\beta_0$is the intercept term of the model;β is the regression coefficient; ε_{it} represents the unobservable values, which are the parts of LST not explained by the vegetation indices and landscape metrics. The common panel data models include three types:

There are three assumptions in the above formula:

(1) When there are no significant differences between individuals over time and cross-sections, it is a pooled regression model, estimated using the Ordinary Least Squares (OLS) method.
(2) When the intercepts of different sections or time series differ, it is a fixed-effects model.
(3) When all individuals have the same intercept term, it is a random-effects model, estimated using Generalized Least Squares (GLS).

To decide whether to use the fixed-effects model or the random-effects model, as shown in Fig. 2, first, under normal circumstances, to prevent spurious regression, all variables need to be tested for unit roots. However, since the data used in the paper has T < N, i.e., the number of periods is less than the number of variables, this test is not required. Then, use the F-test; under the null hypothesis, the individual effects are not significant. If $F < F_{table}$, the hypothesis is rejected, and the pooled effects model is used. If $F > F_{table}$, the hypothesis is accepted, and the fixed-effects model is used. Finally, perform the Hausman test on the fixed-effects model, i.e., the chi-squared statistic (chi^2). By calculating the chi^2 and comparing the estimated values with the true values, a hypothesis test using the chi-squared distribution is conducted. Under the null hypothesis, there should be no significant difference between the parameter estimates. If the test is accepted, the random-effects model is used; if rejected, the fixed-effects model is used.

Method implementation and accuracy evaluation

For image preprocessing and index extraction, this study utilized ArcGIS 10.6, ENVI 5.3, and Fragstat 4.2. Data statistics and model construction were conducted using Eviews 10.2, SPSS, and R software. To evaluate the accuracy of the model, the coefficient of determination (R^2), the root mean square error (RMSE), and the sum of squared errors (SSE) are employed.

Results

Landscape pattern analysis

The calculated results for the changes in landscape indices of various patch types in the urban area of Kunming City from 1995 to 2020 at different scales are shown in Fig. 3. Over time, the patch density (PD) of building

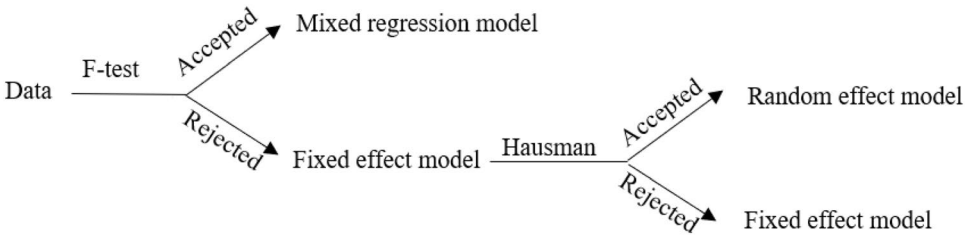

Fig. 2. Process of model selection.

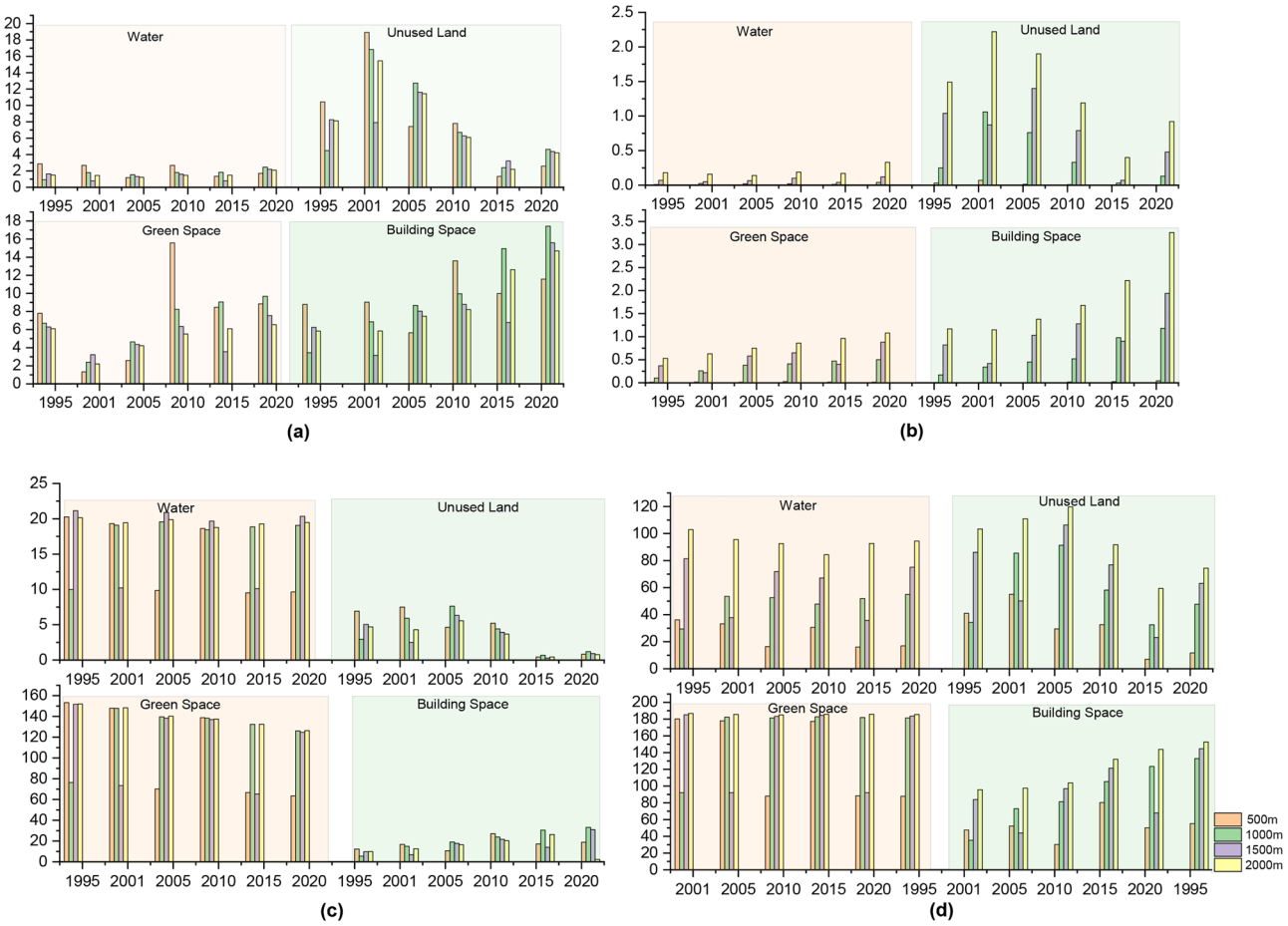

Fig. 3. Calculated changes in landscape index of each patch type in urban areas of Kunming at different scales (**a**: PD, **b**: PAFRAC, **c**: LPI, **d**: COHESION).

spaces has continuously increased, while unused land has shown the opposite trend. The PD of green spaces and water bodies has not changed significantly overall. The changes in the perimeter-area fractal dimension are mainly observed in building spaces and unused land, whereas the changes in LPI are not significant for water bodies. COHESION shows little change in green spaces but is most evident in building spaces. The calculated results for the changes in landscape pattern indices in the urban area of Kunming City from 1995 to 2020 at different scales are shown in Fig. 4. Over time, SHDI and Division have shown an increasing trend, while AI has shown a decreasing trend, indicating that as the city develops, the urban spatial structure becomes more complex and diversified.

LST results and distribution

Using Landsat data, the temperature inferred is the LST, but in regular weather forecasts, the reported temperature is the air temperature. The primary source of heat for air temperature comes from the sun's energy, which is absorbed by the Earth's surface. The surface then transfers heat to the air through radiation, conduction, and convection. This constitutes the primary source of heat for air temperature. The direct absorption of solar radiation by the atmosphere has a minimal effect on warming the air, only causing a temperature increase of 0.015 to 0.02 °C. Therefore, the surface temperature is significantly higher than the air temperature. Based on the results of LST inversion and references to relevant literature, the research results are categorized into five temperature levels: regions with relatively low radiative temperatures, regions with relatively low to moderate radiative temperatures, regions with moderate radiative temperatures, regions with relatively high radiative temperatures, and regions with relatively high radiative temperatures. The classification boundaries are established using 1995 as a standard, with the calculation method being the average value minus 1.5 times the standard deviation, the average value minus 0.5 times the standard deviation, the average value plus 0.5 times the standard deviation, and the average value plus 1.5 times the standard deviation. These values are 11.7 °C, 17.9 °C, 24.1 °C, and 30.4 °C, respectively. The instantaneous thermal field distribution pattern generated according to this is shown in Fig. 5.

Sampling was conducted on the temperature retrievals from MODIS and Landsat data using a 2000 m × 2000 m grid. Following the methodology of Ma Yuhe[43], the average LST for each grid was first calculated for both data sources. Then, the difference in average LST between the two datasets for each grid was determined, and finally,

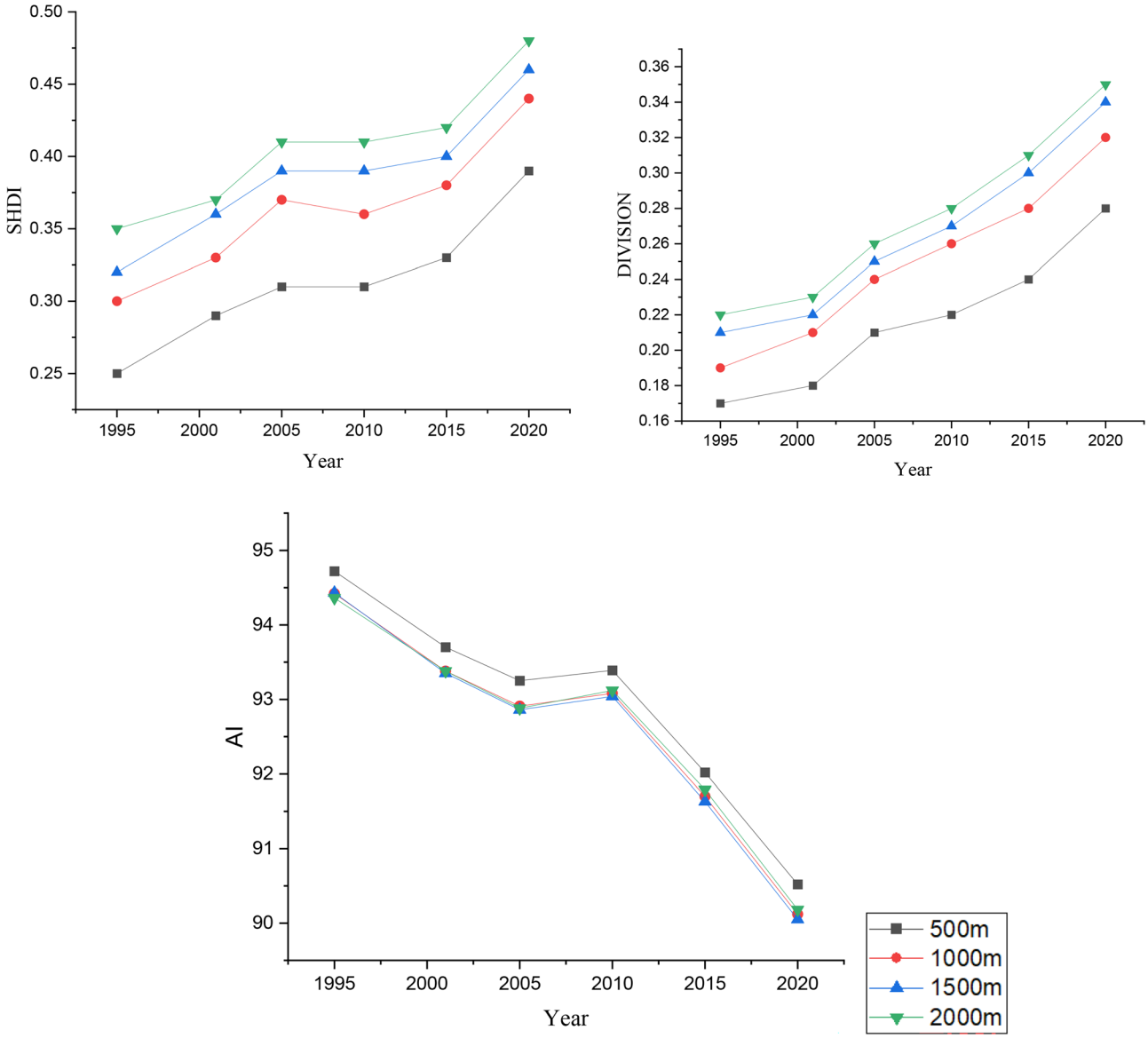

Fig. 4. Landscape pattern index of landscape level at different spatial scales (1995–2020).

the mean temperature difference across all grids was calculated. The results showed that the mean temperature difference between the LST retrieved from Landsat data and that from MODIS data ranged from 1.4 °C to 2.1 °C. The small discrepancy between the two datasets indicates that the retrieved LST is of significant reference value and can meet the needs of subsequent research.

Correlation analysis and final selection of indicators

Panel data were constructed for six periods at four scales (500 m, 1000 m, 1500 m, and 2000 m). The stepwise regression method was employed to eliminate collinearity effects, and simultaneous correlation analysis was conducted. The variables selected at different scales are arranged from left to right as follows: 500 m × 500 m; 1000 m × 1000 m; 1500 m × 1500 m; 2000 m × 2000 m (Fig. 6).

OLS model results

Using LST as the dependent variable, regression equations were established at different scales. The contribution rate of each independent variable to the dependent variable was calculated by dividing the sum of squares of each variable's coefficients by the total sum of squares for each year's regression equation at different scales. As shown in Table 5 and Fig. 7, the R^2 values for all scales are greater than 0.4, indicating that the results of the OLS model are reliable.

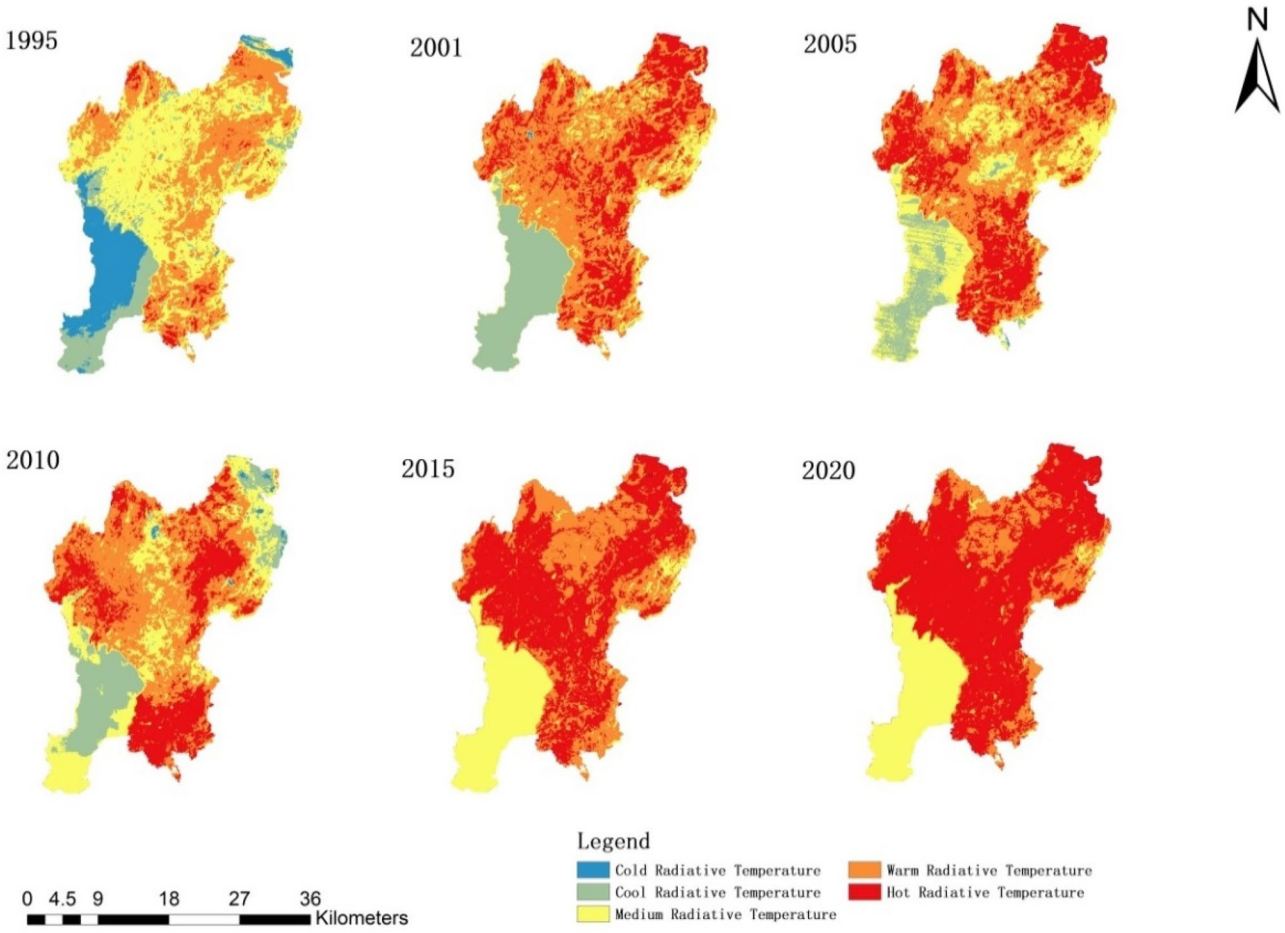

Fig. 5. Instantaneous spatial pattern of thermal force field in Kunming (1995–2020).

Panel data model verification

Panel data were constructed using data from six periods at four scales (500 m, 1000 m, 1500 m, and 2000 m). This paper determines the type of intercept model through the covariance test F value and uses the results of the Hausman test to determine whether the model is a fixed effect or a random effect (Table 6). According to the test results, the final panel data model selects the fixed effect model for regression. That is, the panel data is correlated with individual cross-sections but not with time variables. At the same time, the error term in the model is also correlated with the explanatory variables (Table 7).

Panel data model prediction test

Using data from 1995 to 2015 to forecast the data for the year 2020 is employed to validate the accuracy of the panel data model predictions. The predicted values are then interpolated to obtain a distribution map of surface temperatures (Table 8; Fig. 8). The differences between the maximum, minimum, and average values of the predicted and actual values are quite large, and the predicted values are generally smaller. The RMSE between the predicted and actual values is 5.13, which is much greater than 1, indicating that the model's predictions are poor. The actual LST is mainly characterized by hot radiative temperature areas with a strong UHI effect, whereas the predicted LST is mainly characterized by warm radiative temperature areas. Additionally, anomalies appear in the water body areas, leading to a small portion of these areas showing a warm radiative temperature trend.

Discussion

Figure 3 shows that over the past thirty years, the density of building space patches in Kunming has exhibited an increasing trend at all four scales, indicating a trend towards more fragmented building spaces. The density of green space patches at the 500-meter scale shows a fluctuating trend, decreasing and then increasing. As the sampling scale increases, this trend gradually disappears and tends to be stable, indicating that the spatial structure of green spaces becomes concentrated and then fragmented at small scales but becomes more uniform at larger scales. The PD of water bodies is relatively small and shows little variation at different scales, as the main distribution in Kunming consists of a few large parks and Dianchi Lake, which have undergone minimal changes over the past 25 years. Patches of other land uses show a gradual decrease in density at different scales, indicating that unused land is gradually being replaced by other land uses, resulting in smaller areas and a trend

Fig. 6. Correlation coefficient graph.

Scales	R^2	SSE
500	0.437	690928.5
1000	0.454	166477.3
1500	0.460	77974.3
2000	0.472	41567.6

Table 5. Results of the OLS model

towards fragmentation. For the perimeter-area fractal dimension (PPAFRAC), the green space and water bodies show little change, maintaining similar spatial forms. However, the values for building space and unused land increase with scale, indicating that the scale effect has a greater impact on the morphology of building space and unused land. At larger scales, building space and unused land exhibit more complex boundary features. At the 1500 m and 2000 m grid scales, the values for building space tend to approach 2 over time, while those for unused land tend to approach 1. This indicates that over the past 25 years, the shape of building space patches has become more complex due to land cover changes, whereas unused land has become simpler. The LPI proportion

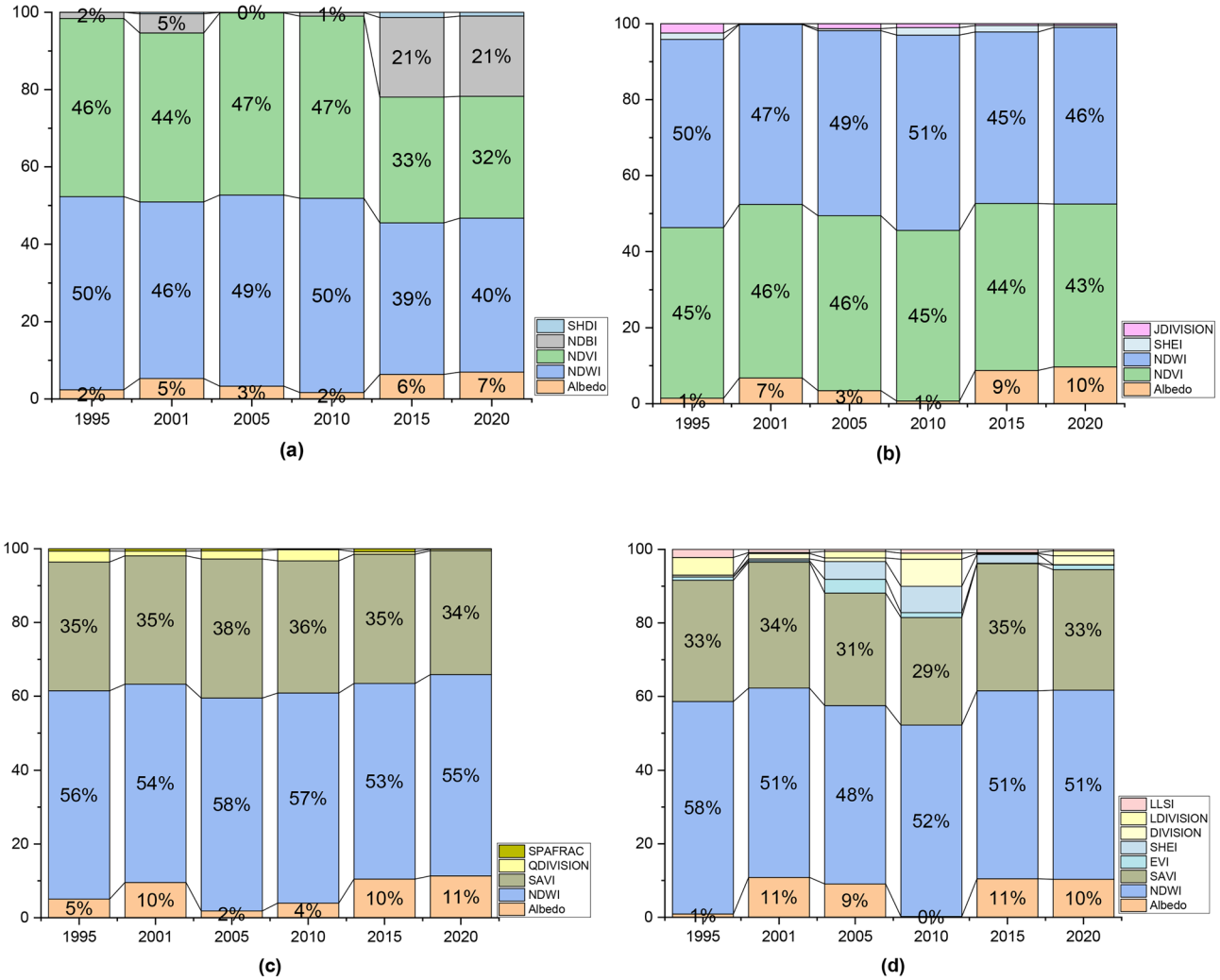

Fig. 7. Contribution rates of independent variables. ((**a**): 500 m × 500 m; (**b**): 1000 m × 1000 m; (**c**):1500 m × 1500 m; (**d**): 2000 m × 2000 m).

Testing method	Scales	Statistics	*p*-value	Results
F-test	500	1.76	< 0.000001	Rejected mixing effect
	1000	1.75	< 0.000001	Rejected mixing effect
	1500	2.21	< 0.000001	Rejected mixing effect
	2000	2.08	< 0.000001	Rejected mixing effect
Hausman-test	500	5806.23	< 0.0001	Fixed-effect model was superior to the random-effect model
	1000	1580.98	< 0.0001	Fixed-effect model was superior to the random-effect model
	1500	1125.34	< 0.0001	Fixed-effect model was superior to the random-effect model
	2000	591.23	< 0.0001	Fixed-effect model was superior to the random-effect model

Table 6. Model selection.

for green spaces and unused land decreases over time at different scales, while water bodies show little change, and the building space proportion gradually increases, demonstrating better overall coherence and dominance. The higher the patch cohesion index (COHESION), the higher the patch connectivity. In this regard, unused land shows a decreasing trend at all four scales, indicating reduced connectivity. Construction land exhibits an increasing trend at all scales, while green spaces show little overall change. For water bodies, connectivity increases with an increase in scale.

As shown in Fig. 4, the number of patches for different types has increased from 1995 to 2020, and the share of each type of patch in the area of landscape elements has changed, leading to a more complex landscape

Scales	Variable	Coefficient	*P*-value	R^2	SSE
500	C	13.642	< 0.001	0.57	471597.1
	ALBEDO	5.573	< 0.001		
	NDWI	-23.143	< 0.001		
	NDVI	-4.738	< 0.001		
	NDBI	6.376	< 0.001		
	JED	0.042	< 0.001		
	SHDI	-2.183	< 0.001		
	SDIVISION	0.509	< 0.001		
	QAI	0.008	< 0.001		
1000	C	13.749	< 0.001	0.59	153424.2
	ALBEDO	6.189	< 0.001		
	GYRATE_MN	-0.004	< 0.001		
	NDVI	-17.15	< 0.001		
	NDWI	-38.348	< 0.001		
	SHEI	-3.865	< 0.001		
	JAREA_MN	0.03	< 0.001		
	JDIVISION	-1.579	< 0.001		
	JED	0.073	< 0.001		
	JLPI	0.036	0.014		
	JPARA_MN	0.001	< 0.001		
	JPLAND	-0.098	< 0.001		
	LLPI	-0.027	< 0.001		
1500	C	8.348	< 0.001	0.6	50006.3
	JED	0.043	< 0.001		
	JPARA_MN	0.001	< 0.001		
	NDWI	-45.786	< 0.001		
	LED	-0.031	< 0.001		
	LLSI	1.122	< 0.001		
	SAVI	-13.432	< 0.001		
	QDIVISION	3.205	< 0.001		
	QGYRATE_MN	-0.030	< 0.001		
	QPARA_MN	-0.002	< 0.001		
	SED	-0.114	< 0.001		
	SPAFRAC	1.094	0.002		
	ALBEDO	4.018	< 0.001		
2000	C	13.919	< 0.001	0.64	26105.7
	JED	0.088	< 0.001		
	JPLAND	-0.15	< 0.001		
	LDIVISION	-6.8	< 0.001		
	LED	-0.141	< 0.001		
	LLSI	2.89	< 0.001		
	SLPI	0.386	< 0.001		
	SPLAND	-0.53	< 0.001		
	ALBEDO	4.136	< 0.001		
	DIVISION	4.565	< 0.001		
	EVI	-1.009	< 0.001		
	NDWI	-35.454	< 0.001		
	SAVI	-8.645	< 0.001		
	SHEI	-2.63	0.018		
	JAREA_MN	0.021	0.001		

Table 7. Regression result. Indices prefixed with "J" represent landscape indices for building space, those prefixed with "L" represent landscape indices for green spaces, those prefixed with "S" represent landscape indices for water bodies, and those prefixed with "Q" represent landscape indices for unused land.

Year	Min	Mean	Max	RMSE
2020	19.32	27.57	44.43	5.13
Predict 2020	8.61	32.00	39.61	

Table 8. Statistical results of actual-predicted values.

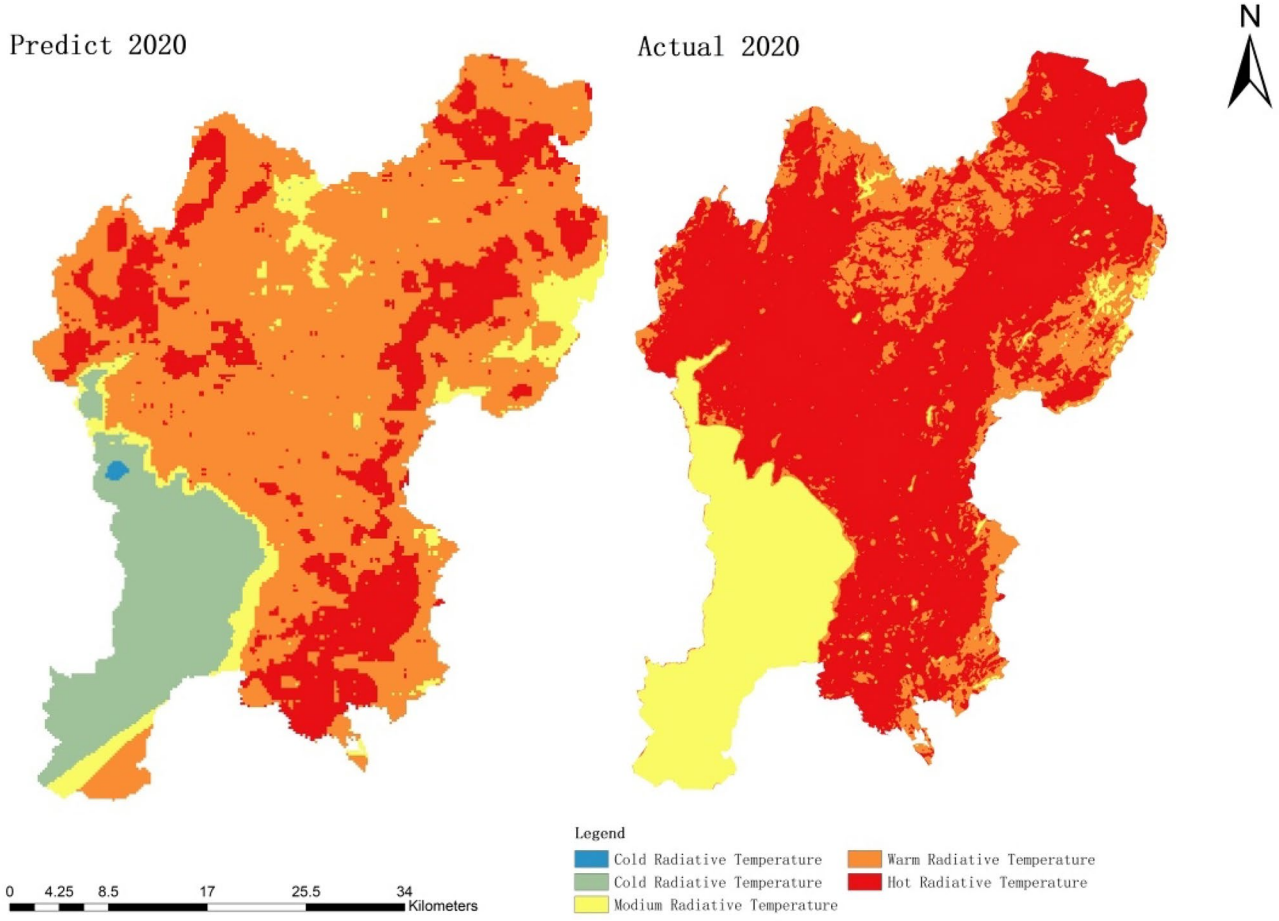

Fig. 8. Predicted surface temperature map for the year 2020.

structure. Additionally, the probability of adjacent patches being of the same type has decreased. Simultaneously, the increase in the number of patches of a certain type has led to a more fragmented and dispersed spatial extension, resulting in an overall increase in landscape fragmentation over the 25 years in the central urban area of Kunming. Analyzing the distribution of various patches, green patches show a gradual decrease followed by a slow increase, while building space expands, covering a larger area with more complex edge shapes.

Figure 5 reflects the variation in LST in Kunming over 25 years. An excessive number of areas with relatively high radiance temperatures indicate adverse urban environmental conditions. In 1995, low-temperature areas were mainly around Dianchi Lake and areas covered by water bodies, with lower temperatures also extending to the forest-covered regions of the Western Hills in Kunming. Moderate-temperature and higher-temperature areas were relatively concentrated in the central urban areas, with only a small portion of high-temperature areas at the edges of Wuhua District and Chenggong District. Over time, the low-temperature area dramatically decreased, becoming sporadically distributed in areas with more forest cover around Kunming. Dianchi Lake and surrounding areas became lower in temperature. Moderate-temperature and high-temperature areas remained concentrated in the central urban areas, gradually expanding. By 2020, low and moderately low-temperature areas had almost disappeared, with Dianchi Lake becoming a moderate-temperature area, and the entire central urban area becoming a high-temperature area, forming a large-scale heat island. The observed pattern of change is consistent with the conclusions of Long Li[44], indicating a significant temporal trend in urban surface heat island intensity. Most cities show a notable increasing trend. The changes in the UHI in Kunming conform to the general patterns of urban transformations. This study, therefore, is replicable for other cities. Additionally, the changes in both LST and landscape pattern indices in 2010 slightly deviated from the overall trend. This could be

attributed to the implementation of the "Grain for Green" policy in Kunming City. The period from 2000 to 2010 was a critical phase for this policy, during which a significant amount of farmland in the study area was covered by vegetation. To some extent, this reduced the overall LST in the study area.

According to Tables 5 and 7, it can observed that the R^2 for the OLS model at each of the four scales is approximately around 0.4, while the R^2 for the panel data model is around 0.6. A higher R^2 indicates a better fit of the model. The SSE between the two models that, for each scale, the SSE of the OLS model is greater than that of the panel data model. Therefore, it can be concluded that the panel data model has higher accuracy and better fitting performance. Additionally, the panel data model incorporates longitudinal comparisons through time series analysis. Achieving this in the OLS model would require modeling for each year, making it time-consuming and resource-intensive.

In the OLS model (Fig. 7), At the 500 m and 1000 m spatial scales, the contribution rates of NDWI and NDVI are the highest, accounting for over 50%. This indicates that water bodies and vegetation are key factors affecting LST. However, as the scale increases, SAVI becomes a better descriptor of vegetation cover compared to NDVI. Therefore, at the 1500 m and 2000 m spatial scales, NDWI and SAVI have the greatest influence on LST. Additionally, with increasing scale, the number of factors influencing LST also increases. Albedo consistently shows a certain contribution rate across all four scales, indicating that solar reflectance is an essential factor affecting LST.

In the panel data model (Tables 5 and 6), at the 500-meter scale, at a significance level of 10%, eight variables, namely ALBEDO, NDWI, NDVI, NDBI, JED, SHDI, QAI, and SDIVISION, passed the test. ALBEDO, NDBI, JED, and SDIVISION show positive correlations with LST, while NDWI, NDVI, and SHDI show negative correlations. Among these, NDWI has the largest elasticity coefficient of -23.143, meaning that a 1% increase in NDWI value leads to a 23.143% decrease in LST. This suggests that an increase in vegetation water content effectively reduces LST. Next are NDBI and Albedo, both with positive impacts on LST, indicating that higher building density and higher solar reflectance result in higher LST. The coefficient for NDVI is -4.738, indicating that richer vegetation leads to lower LST. In terms of landscape pattern indices, SHDI shows a significant correlation, suggesting that a more fragmented landscape within patches has a greater impact on LST. Both QAI, JED, and SDIVISION at the 500-meter scale positively impact LST, but with a relatively small effect.

At the 1000-meter scale, more variables passed the test, with 12 variables including ALBEDO, GYRATE_MN, NDVI, NDWI, SHEI, JAREA_MN, JDIVISION, JED, JLPI, JPARA_MN, JPLAND, and LLPI. NDWI and NDVI have significant impacts on LST, with coefficients higher than at the 500-meter scale. This suggests that when scales become larger, large vegetation distributions occur, which can greatly reduce LST. Solar reflectance remains the most significant factor causing surface warming. Regarding landscape indices, the patch index of building space has a significant impact on LST at this scale, including the average area of building space patches, the separation of building space and other patches, the edge density (ED) of building space, the PD of building space, and the perimeter to area ratios.

At the 1500-meter scale, besides NDWI, which shows a negative correlation as in previous scales, SAVI passed the test. This suggests that, with the scale increasing, SAVI, compared to NDVI, is more sensitive in describing the distribution of vegetation. It can better reflect the influence of vegetation coverage on LST. For the landscape, large patches of unused land appear at this scale, leading to an increased impact on other unused land.

At the 2000-meter scale, NDWI and SAVI remain the most prominent in reducing temperature. Secondly, the separability and shape of green patches have the greatest impact, and the elasticity coefficient of green patches is negative, indicating that as green patches become more fragmented, the temperature reduction becomes less apparent. The landscape shape index (LSI) of green patches is positive, suggesting that irregular shapes of green patches have a greater cooling effect. With the increase in scale, large water bodies appear, and the impact of water bodies becomes significant. The area and proportion of water body patches play a considerable role. Conversely, the size and edge length of the building space patches have the least impact.

Overall, an increase in the proportion of artificial patches (building space, unused land) leads to a higher intensity of the UHI. Conversely, the larger the proportion of natural patches (water bodies, vegetation), the lower the intensity of the UHI. This aligns with previous research, although there are conflicting results regarding the impact of landscape spatial configuration on the UHI. Generally, landscape indices are considered less influential than landscape composition, vegetation indices, and even some socio-economic factors. Therefore, the association patterns between landscape spatial configuration and the UHI obtained in this study are limited to the research area of Kunming. For Kunming, at different scales and with rapidly changing surface patterns, factors such as patch isolation, edge density, and shape are crucial. At the 500-meter scale, the aggregation of building space patches is broken up and concentrated into large and balanced green space patches, which have a good suppression effect on the UHI. At the 1000-meter scale, increasing the aggregation of green patches, mainly achieved through developed land patches, helps alleviate the UHI effect. At the 1500-meter scale, in addition to the influence of green patches, the impact of unused land is also notable. At the 2000-meter scale, increasing the number of water patches and clustering irregularly shaped green space patches can be good ways to mitigate the UHI. Simultaneously, constructing well-formed and concentrated green spaces remains the most effective method for mitigating the heat island effect. Breaking up the aggregation of building space patches is also a promising direction to reduce surface radiation and alleviate the UHI.

The presence of multiple similarly defined variables in the regression model is intended to capture different dimensions of vegetation and landscape pattern characteristics. As shown in Table 6, although NDVI and EVI are important indicators for measuring vegetation status, their effects on LST vary at different spatial scales. At spatial scales of 500 m and 1000 m, NDVI has a significant impact on LST, while EVI only begins to show an effect at a spatial scale of 2000 m. This indicates that, at smaller spatial scales, low to medium vegetation-cover areas have a more pronounced effect on LST. In comparison, at larger spatial scales, the impact of high vegetation-cover areas is more significant. Furthermore, regarding landscape indicators, although both PD and

ED measure the degree of landscape fragmentation, ED has a greater influence on LST than PD across the four different spatial scales. This finding emphasizes the importance of focusing on the length and complexity of landscape edges in mitigating urban heat island effects rather than merely considering the number of patches.

Similarly, the three indicators—LSI, PAFRAC, and PARA_MN—are used to measure the shape complexity of landscape patches, but their effects on LST vary across different land use types. Specifically, LSI significantly affects LST in green spaces, PAFRAC has a more pronounced impact on LST in water bodies, and PARA_MN significantly affects LST in buildings and unused land. These findings suggest that, when mitigating urban heat island effects, attention should be given to the geometric shape characteristics of green spaces, the average shape complexity of buildings and unused land, as well as the self-similarity and morphological changes of water bodies. Therefore, to effectively address this environmental challenge, it is essential to comprehensively consider vegetation cover, landscape fragmentation, and the complexity of patch shapes in optimizing the design and management of green spaces, building spaces, and water bodies.

This study is a promising endeavor to apply economic thought from panel data to address the UHI issue. Previous studies on the UHI have been complex, such as the OLS model requiring separate models for different periods, consuming considerable time, and leading to data redundancy. Panel data effectively addresses these issues. By combining time series and cross-sectional data, panel data provides more information, increases variable variability, reduces collinearity between variables, and improves model effectiveness. Moreover, introducing data from different scales allows the panel data model to capture both local and global features at various scales, making the model more robust and reducing potential errors. By comparing the R^2 (coefficient of determination), RMSE (root mean square error), and SSE (sum of squared errors) of the OLS model and panel data model across different scales, it was found that the panel data model's performance is consistent across scales, showing reasonable regularity. This validates the model's stability and applicability.

Panel data can also better detect and measure effects that cannot be observed using pure cross-section data or time series data. Based on this, predictions of surface radiation levels within different cross-sectional periods can be made. As shown in Table 7, the panel data model's prediction method is not suitable for forecasting the development trend of urban heat islands. The predicted values are generally smaller and show anomalies in water bodies, indicating a high-temperature trend that is opposite to the actual changes.

Given the limitations of the data being confined to the urban area of Kunming, which is in a geographically and climatically unique position, the model needs further refinement. Additional urban data from different terrains and climates should be incorporated to enhance sample diversity. This, however, may lead to a further increase in the sample size of the data, making the use of big data a promising direction for future development. In subsequent studies, efforts will be made to move in this direction accordingly. In addition, when using Landsat satellite imagery to identify small vegetation patches, some small and numerous green spaces may be overlooked due to the resolution of the images. Therefore, in future research, it is necessary to consider adopting optimized image processing and improving image analysis algorithms, such as object-based image segmentation and machine learning algorithms, to address complex scenes and identify small targets, thereby overcoming the limitations of Landsat resolution.

Conclusions

This study utilizes six phases of remote sensing data to invert surface temperature in Kunming City and extracts various vegetation and landscape indices to construct a panel data model for comprehensive analysis. The main conclusions are as follows:

(1) Over a 25-years period, the study analyzes the changes in the landscape pattern of Kunming City at four scales. Within this timeframe, there is a trend towards fragmentation in both building space and unused land, with a significant increase in building space and a gradual decrease in unused land. Under human interference, green space patches show a gradual decrease followed by a slow increase, while overall water bodies undergo minimal change.

(2) Over the same 25-year period, significant changes occurred in Kunming City's thermal field, particularly from 2010 to 2020. High-temperature areas expand rapidly, and low-temperature areas gradually decrease or disappear. Comparative analysis indicates that densely populated areas and industrial clusters release a significant amount of anthropogenic heat, and the resulting impact of landscape pattern changes should not be overlooked.

(3) A total of 20 vegetation indices and landscape indices were extracted for model construction in this study. Considering the results of both the OLS regression model and the panel data model, the panel data model consistently shows the optimal R^2 and SSE values across all scales. Furthermore, the impact of each factor on LST is similar in both models. Therefore, the panel data model is better able to describe the relationship between LST and the various indices. Across different scales, factors influencing land surface thermal radiation vary. Overall, NDWI stands out as the most significant factor, since its cooling effect is becoming more pronounced with increasing scale. NDVI is more effective in describing surface vegetation at smaller scales, while SAVI performs better at larger scales. For landscape indices, at smaller scales, the impact of patch types is minimal, with overall patch fragmentation being the most influential factor. As the scale increases, the impact of building space and unused land patches becomes more apparent, with different effects based on patch area, fragmentation, and edge effects. Green space patches start to exhibit a noticeable cooling effect at scales above 1500 m, with significant cooling observed when large green areas are present. Due to the unique environmental conditions in Kunming, water bodies only demonstrate a high impact at a scale of 2000 m, given the presence of extensive water bodies such as Dianchi Lake.

(4) Low to medium vegetation cover areas at smaller scales and high vegetation cover areas at larger scales have different effects on temperature regulation. At the same time, the geometric shape characteristics of green spaces, the average shape complexity of building space and unused land, and the self-similarity and morphological changes of water bodies all significantly influence LST.

The panel data model is frequently employed in the discipline of economics, but have not been referenced in the context of urban thermal environment studies. Hence, this paper represents a dual exploration of methodology and practice. The results indicate that the method of constructing an urban thermal environment model based on panel data can model the characteristic data with obvious trends such as urban surface irradiance, study the internal law, and help urban planning decision-making, but it is not suitable for long-term prediction. This study is a preliminary attempt, considering only the specific geographic environment of Kunming. Therefore, further investigation is needed to explore patterns of change in different regions over longer periods, requiring additional data supplementation in the future.

Data availability

Sequence data that support the findings of this study are are openly available in https://earthexplorer.usgs.gov/.

Received: 21 June 2024; Accepted: 28 October 2024
Published online: 09 November 2024

References

1. Voogt, J. A. & Oke, T. R. Thermal remote sensing of urban climates. *Remote Sens. Environ.* **86**, 370–384 (2003).
2. Lowe, S. A. An energy and mortality impact assessment of the urban heat island in the US. *Environ. Impact Assess. Rev.* **56**, 139–144 (2016).
3. Smargiassi, A. et al. Variation of daily warm season mortality as a function of micro-urban heat islands. *J. Epidemiol. Community Health*. **63**, 659–664 (2009).
4. Tan, J. et al. The urban heat island and its impact on heat waves and human health in Shanghai. *Int. J. Biometeorol.* **54**, 75–84 (2010).
5. He, B. J. et al. Perception, physiological and psychological impacts, adaptive awareness and knowledge, and climate justice under urban heat: A study in extremely hot-humid Chongqing, China. *Sustainable Cities Soc.* **79**, 103685 (2022).
6. Shepherd, M. The curious relationship between COVID-19 lockdowns and Urban Heat islands. *Geophys. Res. Lett.* **49**, e2022GL098198 (2022).
7. She, Y., Liu, Z., Zhan, W., Lai, J. & Huang, F. Strong regulation of daily variations in nighttime surface urban heat islands by meteorological variables across global cities. (2022).
8. Li, L. et al., *Long-Term and Fine-Scale Surface Urban Heat Island Dynamics Revealed by Landsat Data Since the 1980s: A Comparison of Four Megacities in China. J. Geophys. Res. (Atmospheres)* 127 (2022).
9. Saverino, K. C. et al., *Thermal Inequity in Richmond, VA: The Effect of an Unjust Evolution of the Urban Landscape on Urban Heat Islands.* (2021).
10. Oke, T. R. City size and the urban heat island. *Atmospheric Environ. (1967)*. **7**, 769–779 (1973).
11. Imhoff, M. L., Zhang, P., Wolfe, R. E. & Bounoua, L. Remote sensing of the urban heat island effect across biomes in the continental USA. *Remote Sens. Environ.* **114**, 504–513 (2010).
12. Peng, S., Ciais, P. & Piao, S. Surface Urban Heat Island Across 419 Global Big Cities. *Environmental Science & Technology: ES&T* (2012).
13. Tran, H., Uchihama, D., Ochi, S. & Yasuoka, Y. Assessment with satellite data of the urban heat island effects in Asian mega cities. *Int. J. Appl. Earth Obs. Geoinf.* **8**, 34–48 (2006).
14. Zhou, D., Zhao, S., Liu, S., Zhang, L. & Zhu, C. Surface urban heat island in China's 32 major cities: Spatial patterns and drivers. *Remote Sens. Environ.* **152**, 51–61 (2014).
15. Heinl, M., Hammerle, A., Tappeiner, U. & Leitinger, G. Determinants of urban–rural land surface temperature differences—a landscape scale perspective. *Landsc. Urban Plann.* **134**, 33–42 (2015).
16. Chen, A., Yao, L., Sun, R. & Chen, L. How many metrics are required to identify the effects of the landscape pattern on land surface temperature? *Ecol. Ind.* **45**, 424–433 (2014).
17. Yu, Z., Guo, X., Zeng, Y., Koga, M. & Vejre, H. Variations in land surface temperature and cooling efficiency of green space in rapid urbanization: The case of Fuzhou city, China. *Urban Forestry Urban Green.* **29**, 113–121 (2018).
18. Sun, R. & Chen, L. Effects of green space dynamics on urban heat islands: Mitigation and diversification. *Ecosyst. Serv.* **23**, 38–46 (2017).
19. Jiang, J., Zhou, Y., Guo, X. & Qu, T. Calculation and expression of the urban heat island indices based on GeoSOT grid. *Sustainability* **14** (2022).
20. Sun, R. & Chen, L. How can urban water bodies be designed for climate adaptation? *Landsc. Urban Plann.* **105**, 27–33 (2012).
21. Zhou, W., Huang, G. & Cadenasso, M. L. Does spatial configuration matter? Understanding the effects of land cover pattern on land surface temperature in urban landscapes. *Landsc. Urban Plann.* **102**, 54–63 (2011).
22. Li, X., Zhou, W. & Ouyang, Z. Relationship between land surface temperature and spatial pattern of greenspace: What are the effects of spatial resolution? *Landsc. Urban Plann.* **114**, 1–8 (2013).
23. Li, X., Zhou, W., Ouyang, Z., Xu, W. & Zheng, H. Spatial pattern of greenspace affects land surface temperature: Evidence from the heavily urbanized Beijing metropolitan area, China. *Landscape Ecol.* **27**, 887–898 (2012).
24. Li-Hua, X. U. & Wen-Ze, Y. A study on thermal environment effect of urban park landscape. *Acta Ecol. Sin.* (2008).
25. Shuang, X. U., Feixue, L. I., Luben, Z. & Lei, Z. Spatiotemporal changes of thermal environment landscape pattern in Changsha. 生态学报 (2015).
26. Jia, W. & Zhao, S. Trends and drivers of land surface temperature along the urban-rural gradients in the largest urban agglomeration of China. *Sci. Total Environ.* **711**, 134579 (2020).
27. Li, X. et al. Remote sensing of the surface urban heat island and land architecture in Phoenix, Arizona: Combined effects of land composition and configuration and cadastral–demographic–economic factors. *Remote Sens. Environ.* **174**, 233–243 (2016).
28. Li, J., Zheng, X., Zhang, C., Deng, X. & Chen, Y. How to evaluate the dynamic relevance between landscape pattern and thermal environment on urban agglomeration? *Ecol. Ind.* **138** (2022).
29. Williams, M., Schwarz, P. A., Law, B. E. & Kurpius, M. R. *Improved Analysis of Forest Carbon Dynamics Using Data Assimilation* (Blackwell Science Ltd, 2005).
30. Bera, A. K., Doğan, O., Taşpınar, S. & Leiluo, Y. Robust LM tests for spatial dynamic panel data models. *Reg. Sci. Urban Econ.* **76**, 47–66 (2019).
31. Jin, B., Wu, Y., Rao, C. R. & Hou, L. Estimation and model selection in general spatial dynamic panel data models. *Proc. Natl. Acad. Sci. U.S.A.* **117**, 5235–5241 (2020).
32. Lu, X. & Su, L. Determining individual or time effects in panel data models. *J. Econ.* **215**, 60–83 (2020).
33. Woolridge, J. M. *Econometric Analysis of Cross Section and Panel Data* Vol. 1 206–209 (Mit Press. Books, 2011).
34. Weng, Q., Firozjaei, M. K., Sedighi, A., Kiavarz, M. & Alavipanah, S. K. Statistical analysis of surface urban heat island intensity variations: a case study of Babol city, Iran. *GIScience Remote Sens.* **56**, 576–604 (2019).

35. He, T. et al. Evaluating land surface albedo estimation from Landsat MSS, TM, ETM+, and OLI data based on the unified direct estimation approach. *Remote Sens. Environ.* **204**, 181–196 (2018).
36. Yue, C. Forest Biomass Estimation in Shangri-La Country based on remote sensing. *Beijing Forestry Univ.* (2012).
37. Wang, F. et al. An improved mono-window algorithm for land surface temperature retrieval from landsat 8 thermal infrared sensor data. *Remote Sens.* **7**, 4268–4289 (2015).
38. Li, J. et al. Impacts of landscape structure on surface urban heat islands: A case study of Shanghai, China. *Remote Sens. Environ.* **115**, 3249–3263 (2011).
39. Jin Diandian, G. Z. Algorithms comparison of land temperature retrieval from landsat series data: A case study in Qiqihar. *Remote Sens. Technol. Application*. **33**, 830–841 (2018).
40. Jimenez-Munoz, J. C. et al. Revision of the single-channel algorithm for land surface temperature retrieval from landsat thermal-infrared data. *IEEE Trans. Geosci. Remote Sens.* **47**, 339–349 (2009).
41. Jiménez-Muñoz, J. C. & Sobrino, J. A. A generalized single-channel method for retrieving land surface temperature from remote sensing data. *J. Geophys. Research: Atmos.* **108** (2003).
42. Jiménez-Muñoz, J. C., Sobrino, J. A., Skoković, D., Mattar, C. & Cristóbal, J. Land surface temperature retrieval methods from landsat-8 thermal infrared sensor data. *IEEE Geosci. Remote Sens. Lett.* **11**, 1840–1843 (2014).
43. Yuhe, M. Study on Thermal Environment of Different Land Cover Types in City–A Case Study in Xi'an, Xianyang and Xi Xian New Area. *Northwest University* (2021).
44. Li, L. Analysis of the temporal and spatial characteristics and driving factors of surface urban heat islands in China based on time series decomposition *Nanjing Normal University* (2021).

Author contributions
T.C. original draft preparation and data processing, L.C. data processing and supervision, and correspondent author, Z.R. Supervision and Y.F. review and editing. All authors have read and agreed to the published version of the manuscript.

Funding
The Ten Thousand Talents Program: YNWR-QNBJ-2019-064.

Declarations

Competing interests
The authors declare no competing interests.

Additional information
Correspondence and requests for materials should be addressed to C.L.

Reprints and permissions information is available at www.nature.com/reprints.

Publisher's note Springer Nature remains neutral with regard to jurisdictional claims in published maps and institutional affiliations.